COMMUNICATION

Check for updates

van der Waals solid solution crystals for highly efficient in-air photon upconversion under subsolar irradiance†

Riku Enomoto, [ID] [a] Megumi Hoshi,[a] Hironaga Oyama,[b] Hideki Agata,[c] Shinichi Kurokawa,[d] Hitoshi Kuma,[d] Hidehiro Uekusa[b] and Yoichi Murakami [ID] *[ae]

Triplet-sensitized photon upconversion (UC) has been proposed for broad applications. However, the quest for superior solid materials has been challenged by the poor exciton transport often caused by low crystallinity, a small crystal domain, and aggregation of triplet sensitizers. Here, we demonstrate substantial advantages of the van der Waals solid solution concept to yield molecular crystals with extraordinary performance. A 0.001%-order porphyrin sensitizer is dissolved during recrystallization into the molecular crystals of a blue-fluorescent hydrocarbon annihilator, 9-(2-naphthyl)-10-[4-(1-naphthyl)phenyl]anthracene (ANNP), which contains bulky side groups. This attempt yields millimeter-sized, uniformly colored, transparent solid solution crystals, which resolves the long-standing problem of sensitizer aggregation. After annealing, the crystals exhibit unprecedented UC performance (UC quantum yield reaching 16% out of a maximum of 50% by definition; excitation intensity threshold of 0.175 sun; and high photostability of over 150 000 s) in air, which proves that this concept is highly effective in the quest for superior UC solid materials.

New concepts

Herein, the concept of van der Waals solid solutions has been demonstrated to yield triplet-sensitized photon upconversion (UC) organic crystals with extraordinary performance. The use of a hydrocarbon annihilator with bulky side groups (ANNP), which we discovered to embody this concept, has been shown to dissolve triplet-sensitizing porphyrins into the crystals of ANNP during recrystallization and generate uniformly colored and transparent crystals, which are solid solutions we aimed towards. The large conformational freedom of the side group in the crystal is elucidated to be the key to generate solid solutions. Near-equilibrium formation of only the α-phase (ANNP crystal doped with sensitizer molecules) without generating the β-phase (sensitizer aggregates) differentiates this concept from the existing kinetically controlled concept that causes a small crystal domain size and a short exciton diffusion length. The present concept effectively enhances the lifetime and diffusion length of triplet excitons because of the high crystallinity. After annealing, the crystals exhibit outstanding UC performance in air, which demonstrates the effectiveness of this concept. Suppression of the detrimental back energy transfer from the annihilator to the sensitizer has been shown to be an additional advantage. Therefore, the proof-of-concept here opens a large domain of versatile dispersion-force-based organic systems in the quest for superior UC solids.

Introduction

Photon upconversion (UC) creates high-energy photons that are useful for many purposes from less-useful, longer-wavelength photons. UC based on triplet–triplet annihilation (TTA) is an active area of research because of broad applicability spanning

[a] *School of Engineering, Tokyo Institute of Technology, 2-12-1 Ookayama, Meguro-ku, Tokyo 152-8552, Japan. E-mail: murakami.y.af@m.titech.ac.jp*

[b] *Department of Chemistry, Tokyo Institute of Technology, 2-12-1 Ookayama, Meguro-ku, Tokyo 152-8551, Japan*

[c] *Nissan Motor Co., Ltd., 2 Takaracho, Kanagawa-ku, Yokohama, Kanagawa 220-8623, Japan*

[d] *Idemitsu Kosan Co., Ltd., 1-2-1 Otemachi, Chiyoda-ku, Tokyo 100-8321, Japan*

[e] *PRESTO, JST, 4-1-8 Honcho, Kawaguchi, Saitama 332-0012, Japan*

† Electronic supplementary information (ESI) available. CCDC 2109297–2109300. For ESI and crystallographic data in CIF or other electronic format see DOI: 10.1039/d1mh01542g

solar energy harvesting,[1–3] optoelectronics,[4,5] photochemistry,[6–8] photoelectrochemistry,[9–11] and bio-related applications.[12,13]

To date, the majority of reports on TTA-UC have studied liquid samples.[1–3] However, liquid samples have risks of freezing, evaporation, and ignition, although some samples have high stability even against a flame.[14,15] Furthermore, the large gas diffusivity in liquids requires suppression of damaging singlet oxygen.[12,16–18] To resolve these issues, a solid UC system is being quested[19–22] where triplet energy transfer (TET) from the sensitizer to the annihilator and triplet exciton diffusion should be efficiently designed (Fig. 1a).

After some initial works,[23–28] the major obstacle has been the segregation of the sensitizer from the condensed phase of the annihilator,[29–38] which forms an aggregate of the sensitizer and greatly diminishes the UC quantum yield (Φ_{UC}, defined as
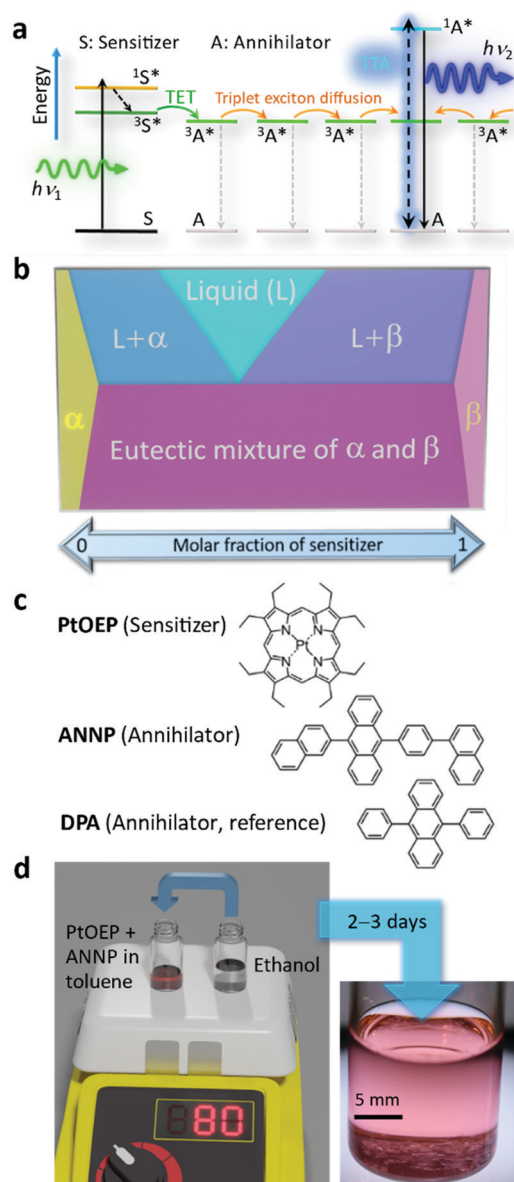
Fig. 1 (a) Schematic energy diagram illustrating TTA-UC where triplet excitons in the annihilator diffusively migrate until they undergo a TTA or nonradiative decay to the ground state. (b) Schematic phase diagram of a two-component system with limited mutual solubility, where α and β represent solid solutions. The concept of the present study is to selectively generate a dispersion-force-based α solid solution where a small quantity of sensitizer is dissolved in the crystal of the annihilator. (c) Molecular structures of PtOEP, ANNP, and DPA. (d) Schematic of sample preparation and a typical photograph taken after 3 days of crystal growth in a screw cap glass vial, where transparent crystals are evident at the bottom.

a maximum of 50% in this report), as typically reported for the combination of platinum octaethylporphyrin (PtOEP, Fig. 1b) and 9,10-diphenylanthracene (DPA, Fig. 1b).[29–33]

To avoid this segregation issue, previous studies used a kinetically controlled approach[30–38] where organic solids were quickly formed. For example, Simon and coworkers[30] reported the fabrication of molecular glasses by rapidly cooling a hot melt of a sensitizer–annihilator mixture, but suppression of the

aggregate was incomplete. Other studies[31–38] formed organic thin films by casting a solvent solution on a flat substrate, where researchers, to an effective extent, suppressed the segregation of the sensitizer from the annihilator chromophores.

Some mechanistic studies showed, however, that the grain boundary and thus the grain size were the limiting factors for triplet exciton diffusion.[39,40] Mikhnenko et al.[41] pointed out a significant degree of disorder in amorphous and polycrystalline organic thin films, in particular when the films were cast from solution.

Although the number of reports is limited, some studies used nonkinetic approaches.[13,42–45] For example, Oldenburg et al.[42] fabricated sensitizer–annihilator heterojunctions of thin metal–organic framework (MOF) layers and reported $\Phi_{UC} < 0.1\%$ and an excitation threshold intensity‡ (I_{th}) of ca. 1 mW cm^{-2}. Ogawa et al.[43] reported an aggregation-free dispersion of an anionic sensitizer in the crystal of an ionic annihilator utilizing ionic interactions between the chromophores ($\Phi_{UC} = 3\%$ and $I_{th} = 49$ mW cm^{-2} in Ar), in which the photographs of the crystals, photostability data, and information on whether or not the crystals included the solvent methanol were not presented. Recently, Roy et al.[45] reported MOF crystals with $\Phi_{UC} = 1.95\%$ and $I_{th} = 5.1$ mW cm^{-2}. However, these values were, as in other MOF-based reports,[13,44] for a liquid suspension and no photostability data were shown, whereas ref. 13 ($\Phi_{UC} = 0.64\%$ and $I_{th} = 2.5$ mW cm^{-2}) showed photodegradation data.

Surprisingly, van der Waals crystals formed by dispersion forces, representing the simplest class of organic crystals, have been nearly unexplored in the quest for high-performance UC solids. This lack of study may be because of the impact of the initial work[29] that showed considerable segregation of PtOEP from the molecular crystal of DPA, which was also found in subsequent reports;[30–33] the authors of ref. 43 described that dispersion-force based strategies sacrifice the advantages of crystalline systems.

The dispersion force approach has, however, many inherent advantages. First, by use of a weak dispersion force, the cost of the chromophores can be minimized because there is no need for elaborate moieties or ligands that cause specific interactions. Second, by use of a defined phase, samples can gain thermodynamic stability. This is in contrast with the previous strategy of using kinetically controlled methods because solids formed by such rapid methods rely on a nonequilibrium state.

Herein, we show, to our best knowledge, the first explicit exploitation of van der Waals forces to unequivocally resolve the long-standing sensitizer segregation problem by means of the classical but resurging concept of *solid solutions*.[46] In solid solutions, represented by α and β phases in Fig. 1b, mixing entropy is the driving force that molecularly disperses one component into a solid of the other component.[46,47] Thus, the strategy envisaged here is to selectively generate dispersion-force-based α crystals and avoid emergence of a β phase that is the sensitizer aggregate (Fig. 1b). We generated such solid solution crystals with an extremely low sensitizer : annihilator mole ratio (ca. 1 : 50 000). Note that the similar term *mixed crystal* can include heterogeneous systems, such as a mixture of α and β phases,[47] which was not targeted here.

One of the key factors of the success here is attributable to our discovery of an excellent hydrocarbon annihilator, 9-(2-naphthyl)-10-[4-(1-naphthyl)phenyl]anthracene (ANNP, Fig. 1c), originally developed as a blue organic light-emitting diode (OLED) chromophore. Researchers often choose an asymmetric structure in OLED molecules.[48,49] The key mechanism responsible for successful formation of α-phase crystals is attributable to the 4-(1-naphthyl)phenyl side group, which features two distinct conformations and provides an interstitial site in the crystal. The sample was generated by a recrystallization method (Fig. 1d and Experimental section, ESI†) over 2–3 days. We thereby generated crystals that display extraordinary performance in air, as shown below.

Results and discussion

The crystals were pinkish (color of PtOEP) and transparent (Fig. 2a), with a flat-plate shape and thickness between *ca.* 50 and 250 μm (Fig. 2b). Polarization microscopy indicated twin-like multiple single-crystalline domains (Fig. 2b). The results were highly reproducible and we found no polymorph.

Optical absorption measurements of a crystal were straightforward because of the flat shape (Fig. S1, ESI†). The absorption spectrum of the single crystal (Fig. 2c) was identical to that of a dilute toluene solution of PtOEP, albeit with a 3.5 nm redshift of the peak. Fig. 2c also shows a spectrum of an over-saturated suspension of PtOEP in toluene, exhibiting an aggregation feature at 550 nm.[50,51] The absence of the aggregation feature in the UC crystal indicates molecular dissolution of PtOEP in the crystal of ANNP and thus formation of a solid solution. Optical microscopic observations at a high magnification did not indicate aggregates (Fig. S2, ESI†). The spectrum did not depend on the light polarization (Fig. S3, ESI†) and thus PtOEP had no preferential orientation, at least for the direction normal to the largest crystal plane. From the absorption spectra, the concentration of PtOEP in the crystals was *ca.* 5×10^{-5} M (Table S1, ESI†). This corresponds to a significantly low sensitizer : annihilator mole ratio of *ca.* 1 : 50 000, which also supports that the crystals in Fig. 2 are a solid solution.

Below, we conducted all of our experiments in air. We excited the samples with a laser at 542 nm, which was 3.5 nm away from the absorption peak at 538.5 nm (Fig. 2c), unless otherwise stated. In this report, an excitation of 1 mW cm^{-2} intensity at 542 nm corresponds to a sensitizer excitation density[52,53] of *ca.* 4.8×10^{-5} M s^{-1}. We used a microscope-based setup (Fig. S4, ESI†) to investigate the photoemission from a single crystal.

During excitation at 542 nm, we observed an UC emission peaked at 434 nm (Fig. 3a). Conversely, we observed no UC emission from a reference crystal prepared with DPA by the same method (Fig. 3a and S5, ESI†). This demonstrates that the side groups of ANNP (Fig. 1c) played a key role in accommodating PtOEP in the crystal, as discussed below. The quantum yield of the phosphorescence of PtOEP (inset of Fig. 3a) was *ca.* 1×10^{-5}, indicating that the TET from PtOEP to ANNP was quantitative.

Notably, we greatly enhanced the emission intensity (Fig. 3a), Φ_{UC} (Fig. 3b), and I_{th} (Fig. 3c) of the as-generated crystals by annealing at 90 °C for 4 days to Φ_{UC} = 16.4% and I_{th} = 0.77 mW cm^{-2} for the maximum and lowest values, respectively, for measurements of 10 samples. The average values were 13.4% and 2.1 mW cm^{-2}, respectively; Table S1 and Fig. S6 and S7 (ESI†) present the entire data. This dramatic enhancement is attributable to the improved crystallinity, as supported by the selective increase of the intensities of higher-angle peaks in the powder X-ray diffraction patterns by annealing (Fig. S8, ESI†). This hypothesis is further supported by the drastic increase of the triplet lifetime τ_T from a value of 470 μs to a value of 5.1 ms (Fig. 3d). We also found a slight increase in the fluorescence quantum yield Φ_{FL} (from a value of 38.7% to a value of 41.7%, Table S2, ESI†). Note that these values were lower than the Φ_{FL} of ANNP in a toluene solution (3×10^{-6} M, deaerated by three freeze–pump–thaw cycles), which was measured to be 84.3%; refer to Fig. S9 in the ESI† for the fluorescence spectra of ANNP in the crystal and toluene solution. Therefore, Φ_{UC} in the present materials system is largely limited by Φ_{FL} in the crystalline state.

In Fig. 3c, we regarded 2.31 mW cm^{-2}, obtained by integrating an AM1.5 solar spectrum[54] over the range of 538.5 ± 7 nm, as an equivalent solar irradiance for monochromatic excitation at 542 nm ($\odot_{542nm}$) based on eqn (1):

$$\varepsilon_{542\,nm} \cong \frac{1}{545.5 - 531.5} \int_{531.5}^{545.5} \varepsilon_\lambda d\lambda, \qquad (1)$$

Fig. 2 Morphological and optical absorption properties of the UC crystals. (a) Digital photographs of the crystals. (b) Micrographs of typical crystals and the corresponding images under a polarization microscope. Their thicknesses were 56 μm (left) and 118 μm (right). (c) Optical absorption spectra of a UC crystal (blue, crystal thickness: 242 μm), a dilute toluene solution of PtOEP (black dash, 6×10^{-5} M), and an over-saturated toluene suspension of PtOEP (orange, greater than 2×10^{-3} M). Here, we normalized the peak absorbance values of the solutions to that of the UC crystal. The asterisk and arrow indicate the absorption feature of the aggregate of PtOEP and the excitation wavelength (542 nm), respectively.
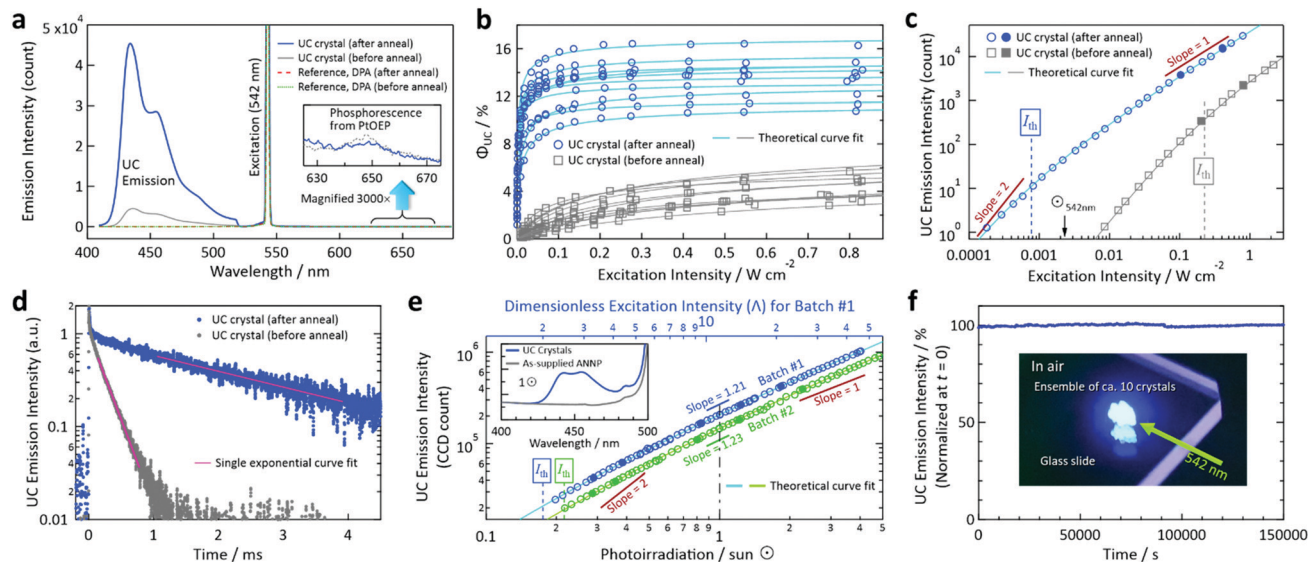
Fig. 3 Photoemission properties measured in air. (a) Typical emission spectra acquired from a UC crystal before and after annealing. For comparison, we show the results of a reference crystal prepared with DPA (Fig. S5, ESI†), from which we observed no UC emission. The inset shows a 3000× magnification of the 625–675 nm range. (b) Dependence of Φ_{UC} on the excitation intensity at 542 nm acquired from 10 crystals for the cases of before and after annealing. Refer to Table S1 (ESI†) for the entire dataset for the 20 crystals in total. (c) Dependence of the UC emission intensity on the excitation intensity at 542 nm acquired from samples #A7 and #B2 in Table S1 (ESI†) (refer also to Figs. S6 and S7, ESI†). We fit the curves by a theoretical function (ref. 53), from which we obtained I_{th} values. (d) Time-resolved UC emission intensity decay curves (excitation: 540 nm, monitor: 455 nm) acquired from an ensemble of ca. 10 UC crystals before and after annealing. Note that the triplet lifetime τ_T is twice the decay time-constant of the UC emission intensity. (e) Dependence of the UC emission intensity on the simulated sunlight irradiance in units of sun (⊙) to an ensemble (3.2 mg) of the UC crystals. Refer to the Experimental section for details. The inset shows the emission spectra acquired under 1⊙ irradiance after being passed through a 510 nm long-pass filter, where the results obtained with the as-supplied ANNP powder (3.2 mg) are also presented. (f) Photostability test under continuous irradiation of 542 nm laser light (intensity: 20 mW cm⁻²) to an ensemble of ca. 10 UC crystals on a glass slide, as shown by the inset photograph acquired through a notch filter. We corrected the fluctuation of the excitation laser power during the measurement (refer to Fig. S14, ESI†). In panels (c) and (e), we acquired the data represented by open marks first by increasing the excitation light power, and then we acquired the data represented by filled marks to check the quantitative reproducibility.

in the spectrum shown in Fig. 2c, where ε_λ is the molar absorption coefficient of PtOEP in the crystal at wavelength λ. However, such an equivalent irradiance has an unclear meaning, which can be also recognized by the lack of a clear definition for it.[52] One clear problem of such ⊙ ₅₄₂nm is that it cannot include ε_λ that is outside the integration range of eqn (1).

We thus resort to direct evaluation using a solar simulator. We passed the simulated sunlight through a 510 nm long-pass filter and irradiated onto an ensemble (3.2 mg) of the crystals (batch #1) (Experimental section and Fig. S10, ESI†). We obtained the UC emission from the sample under one-sun (1⊙) irradiance, whereas we observed no emission when we replaced the crystals by the same quantity of ANNP (inset of Fig. 3e). This verified that the blue fluorescence exclusively originated from UC. From the dependence of the UC emission intensity on the irradiance (Fig. 3e), the slope in the double-logarithmic scale was 1.21 at 1⊙. Using this slope, we calculated the dimensionless excitation intensity[53] (Λ) to be 11.1 at 1⊙. Because this is well above the value $\Lambda = 2$ that corresponds to I_{th},[53] we have confirmed the subsolar nature of the present UC. The theoretical curve fit[53] to the data points yielded $I_{th} = 0.175$⊙, which matched $\Lambda = 2$ as shown by the top axis of Fig. 3e. This I_{th} value is unprecedentedly low.

The reproducibility check carried out using another sample batch (batch #2, 3.2 mg) reproduced the results with a slightly different $I_{th} = 0.216$⊙.

There are two additional features of the crystals. First, the crystals exhibit high photostability under continuous photoirradiation in air (Fig. 3f, at 542 nm and 20 mW cm⁻²). Such photostability may come from the close-packed molecular arrangement that is attributable to the high crystallinity. Second, thermo-gravimetric analysis (TGA) showed that the crystals contained 2.1 wt% solvent, and this quantity did not change by annealing (Fig. S11, ESI†). This indicates stable accommodation of the solvent, which can escape at a temperature greater than 150 °C (Fig. S11, ESI†).

We analyzed single-crystal X-ray diffraction (sc-XRD) data for a single crystal of the as-received ANNP (Fig. 4a) and a single domain cut out of the UC crystal (Fig. 4b). For the latter, only the case after annealing is shown here because the change in the crystallographic parameters caused by annealing is too small to be clearly evident pictorially (see Table S3 for these crystallographic data, ESI†). In Fig. 4b, PtOEP is not seen because of its significantly low concentration.

These data indicate that the 2-naphthyl group had two slightly different conformations, displayed in green and light pink whose ratio was 72 : 28 for both Fig. 4a and b. Conversely,

Fig. 4 Crystal structures determined from the single crystal X-ray diffraction data. (a) As-supplied ANNP and (b) UC crystal after annealing. Here, the side groups of ANNP have two distinct conformations (4-(1-naphthyl)phenyl group in light blue and orange, and 2-naphthyl group in green and light pink) that coexist in both cases. In panel (b), ethanol molecules are shown in magenta. Refer to Table S3 (ESI†) for the crystallographic data for all the cases. CCDC deposition numbers 2109297 and 2109300 contain the supplementary crystallographic data for panels (a) and (b), respectively.

the 4-(1-naphthyl)phenyl group had two substantially different conformations, displayed in light blue and orange whose ratio was 51 : 49 for both Fig. 4a and b. As evident in the center of the graphics, simultaneously adopting light-blue configurations by two adjacent ANNP molecules is prohibited because of their spatial overlap. Only "light blue + orange" or "orange + orange" pairs are allowed. This large conformational freedom suggests the presence of an interstitial space near it.

We discuss two notable points. First, as shown in Fig. 4b, there are ethanol molecules, shown in magenta color, near this conformational freedom with a mole ratio of ANNP : ethanol = 5 : 1. This ratio did not change by annealing, which agrees with the constant quantity of the included solvent (2.1 wt%) by annealing found by TGA. Here, 2.1 wt% ethanol corresponds to the mole ratio of ANNP : ethanol $\cong$ 4 : 1, which roughly agrees with the ratio determined by the sc-XRD analysis. Second, the crystal structure of the UC crystal did not change from that of the as-supplied ANNP, except for slight changes in the crystallographic parameters (Table S3, ESI†). This implies the rigidity of the ANNP arrangement in the crystal. From the sc-XRD data, the density of ANNP was 2.44×10^3 mol m^{-3}, which is much lower than those of anthracene (6.99×10^3 mol m^{-3})[55] and DPA (3.72×10^3 mol m^{-3}).[56] We surmise that PtOEP molecules were also accommodated near that side group, although not directly evident by this analysis. Thus, the rigid and low-density network of ANNP and the movable 4-(1-naphthyl)phenyl side group are the key factors for realizing the concept we targeted. Notably, analysis of the sc-XRD data assuming toluene instead of ethanol was impossible. However, a trace quantity of toluene could have also been included. The inclusion of a much lesser quantity of toluene could be ascribed to the larger molecular volume of toluene in organic crystals (Voronoi–Dirichlet polyhedron volume, 157.5 Å^3) than that of ethanol (86.4 Å^3).[57]

Triplet exciton diffusion characterizes the properties of a solid TTA-UC system.[41,58] Monguzzi et al. derived[59]

$$I_{th} = \frac{1}{\alpha \Phi_{TET} 8\pi a_0 D_T \tau_T^2}, \quad (2)$$

where α is the sensitizer absorption coefficient at the excitation wavelength, Φ_{TET} is the quantum efficiency of the TET (assumed to be unity), a_0 is the minimum distance required for the annihilation of two annihilator triplets, and D_T is the diffusion coefficient of the triplet exciton. For a_0, we used the average value of the nearest-neighbor and second-nearest neighbor distances (7.44 and 8.84 Å, respectively, Fig. S12, ESI†). Using the average value of I_{th} for monochromatic excitation at 542 nm (2.1 mW cm^{-2}), α (3.5×10^{-3} cm^{-1}), and τ_T (5.1 ms), D_T was 9.22×10^{-7} cm^2 s^{-1}. The triplet exciton diffusion length L_T is given by[41,58]

$$L_T = \sqrt{2ZD_T\tau_T}, \quad (3)$$

where Z is the dimensionality (from 1 to 3). We assume $Z = 3$, although this must be elucidated by future work. Depending on the custom, the other form

$$L'_T = \sqrt{ZD_T\tau_T}, \quad (4)$$

is also used.[41,58] From these relations, the present UC crystals have an L_T (L'_T) of 1.68 (1.19) μm. These values are approximately two orders of magnitude larger than the previously reported values for solid TTA-UCs,[13,40,60,61] except L_T ~1.6 μm for water-suspended MOF nanoparticles of ca. 55 nm size.[13] We compared these reported L_T and D values in Table S4 (ESI†). Thus, within a sphere with radius L_T (L'_T), there are approximately 1.25×10^6 (4.43×10^5) PtOEP molecules. Therefore, the significantly low concentration of PtOEP caused by our use of the α-phase (cf. Fig. 1b) was not problematic. These results reconfirm previous suggestions[39,40,43] that high crystallinity and a large crystalline domain are important for efficient UC in solids.

Finally, we discuss back-energy transfer (BET, Fig. 5a). BET was previously regarded as inevitable in a binary sensitizer–annihilator solid based on the estimated BET efficiency (Φ_{BET}) as high as 40%.[35] When Förster resonance energy transfer (FRET)[62] is the dominant mechanism, Φ_{BET} can be estimated by comparing the fluorescence decay time-constant (τ_{1A}) from

Fig. 5 Investigation of BET from the excited singlet annihilator $^1A^*$ to the ground state sensitizer S. (a) Schematic energy diagram of BET, where $k_{1A(rad)}$ and $k_{1A(nonrad)}$ refer to the radiative and non-radiative decay rates of $^1A^*$, respectively, and $k_{1A(BET)}$ refers to the rate of BET by the Förster mechanism. (b) Time-resolved fluorescence intensity decay curves (excitation: 405 nm, monitor: 455 nm) for the UC crystals (blue) and reference crystals prepared without PtOEP (pink). We generated these curves by averaging the curves acquired from 10 crystals for each case. We multiplied the data for the "UC crystal" by 1.21 to match the heights of these curves at time = 0.

the UC crystals and τ_{1A} from the crystals prepared without PtOEP (Fig. 5b). Note that this method cannot be used to evaluate the BET caused by simple reabsorption of UC photons by the sensitizer because this reabsorption does not change τ_{1A}. Thus, here we assess the BET by FRET that actively quenches the $^1A^*$ state. Our double-exponential fits in Fig. 5b yielded fast and slow components, where the time-constants were 2.50 and 7.04 ns for the UC sample, and 2.45 and 7.18 ns for the reference, respectively. These small differences are considered to have mostly arisen from the uncertainty in the curve fitting. Thus, Φ_{BET} in the present system is negligible because of the low concentration of PtOEP. We mention that the τ_{1A} of ANNP in a toluene solution (3×10^{-6} M, deaerated by three freeze–pump–thaw cycles) was 3.78 ns (Fig. S13, ESI†), which was similar to τ_{1A} for the crystals.

Conclusions

We demonstrated the concept of explicitly exploiting van der Waals solid solution crystals consisting of only an α-phase to resolve the long-standing problem of sensitizer segregation and realize materials with outstanding UC performance. Compared with the existing concept of using kinetically controlled fast-solidification conditions, the present approach has the

advantages of (i) higher thermodynamic stability because of the reliance on (near-)equilibrium states and (ii) higher UC performance because of the simultaneous achievements of a long triplet exciton diffusion length and suppression of detrimental BET from the $^1A^*$ states. The factors in (ii) were caused, respectively, by the large single-crystal domain with high crystallinity and the significantly low concentration of the sensitizer. To form crystalline solid solutions, the interstitial site created by the bulky and movable side group of ANNP has been found to be the key factor, as supported by the comparison with a reference crystal prepared with DPA. The elucidated high Φ_{UC}, low I_{th}, and high photostability in air are promising for applications. In particular, the extraordinarily low I_{th} demonstrated by using simulated sunlight indicates that solar concentration optics are no longer needed for efficient upconversion of terrestrial sunlight. Probably the most important advantage of this concept lies in its reliance on the versatile van der Waals force and hydrocarbon annihilators. Overall, the proof-of-concept here is a major technical leap forward in the quest for high-performance UC solids, which will open up diverse photonics technologies in the future.

Author contributions

Y. M. conceived the idea and supervised the project. Y. M., H. A., S. K., and H. K. led the project. R. E. and M. H. performed the experiments and analyzed the data. H. K. and S. K. contributed to searching for and selecting the annihilator. R. E. conducted single-crystal X-ray diffraction measurements. H. U. and H. O. analyzed the diffraction data and determined the crystal structure. Y. M. and R. E. wrote the manuscript. All authors commented on the manuscript and agreed with the submission of this manuscript.

Conflicts of interest

There are no conflicts to declare.

Acknowledgements

Notes and references

‡ When calculating I_{th}, the definition of the laser spot area is important. Some researchers used the $1/e^2$ diameter to calculate the spot area for Gaussian laser beams. However, as described in ref. 63, the laser spot area calculated by the $1/e^2$ diameter yields a 50% lower excitation intensity than the actual peak intensity in the laser spot. In all previous TTA-UC papers authored by Y. M., a FWHM diameter of the Gaussian profile was used to calculate the spot area, yielding a 1.44 times higher intensity than the actual peak intensity; i.e., conservative calculation of I_{th}. In the present article, however, all excitation beams had a top-hat intensity profile (cf. Fig. S4, ESI†), and therefore the intensity values for

all laser-based experiments matched the actual excitation intensity on the sample.

1　S. Baluschev, T. Miteva, V. Yakutkin, G. Nelles, A. Yasuda and G. Wegner, *Phys. Rev. Lett.*, 2006, **97**, 143903.

2　V. Gray, D. Dzebo, M. Abrahamsson, B. Albinsson and K. Moth-Poulsen, *Phys. Chem. Chem. Phys.*, 2014, **16**, 10345–10352.

3　T. F. Schulze and T. W. Schmidt, *Energy Environ. Sci.*, 2015, **8**, 103–125.

4　K. Börjesson, P. Rudquist, V. Gray and K. Moth-Poulsen, *Nat. Commun.*, 2016, **7**, 12689.

5　R. Ieuji, K. Goushi and C. Adachi, *Nat. Commun.*, 2019, **10**, 5283.

6　B. D. Ravetz, A. B. Pun, E. M. Churchill, D. N. Congreve, T. Rovis and L. M. Campos, *Nature*, 2019, **565**, 343–346.

7　A. Tokunaga, L. M. Uriarte, K. Mutoh, E. Fron, J. Hofkens, M. Sliwa and J. Abe, *J. Am. Chem. Soc.*, 2019, **141**, 17744–17753.

8　B. Pfund, D. M. Steffen, M. R. Schreier, M. S. Bertrams, C. Ye, K. Börjesson, O. S. Wenger and C. Kerzig, *J. Am. Chem. Soc.*, 2020, **142**, 10468–10476.

9　R. S. Khnayzer, J. Blumhoff, J. A. Harrington, A. Haefele, F. Deng and F. N. Castellano, *Chem. Commun.*, 2012, **48**, 209–211.

10　H. Kim, O. S. Kwon, S. Kim, W. Choi and J. H. Kim, *Energy Environ. Sci.*, 2016, **9**, 1063–1073.

11　M. Barawi, F. Fresno, R. Pérez-Ruiz and V. A. de la Peña O'Shea, *ACS Appl. Energy Mater.*, 2019, **2**, 207–211.

12　Q. Liu, B. Yin, T. Yang, Y. Yang, Z. Shen, P. Yao and F. Li, *J. Am. Chem. Soc.*, 2013, **135**, 5029–5037.

13　J. Park, M. Xu, F. Li and H. C. Zhou, *J. Am. Chem. Soc.*, 2018, **140**, 5493–5499.

14　Y. Murakami, Y. Himuro, T. Ito, R. Morita, K. Niimi and N. Kiyoyanagi, *J. Phys. Chem. B*, 2016, **120**, 748–755.

15　Y. Murakami, S. K. Das, Y. Himuro and S. Maeda, *Phys. Chem. Chem. Phys.*, 2017, **19**, 30603–30615.

16　F. Marsico, A. Turshatov, R. Peköz, Y. Avlasevich, M. Wagner, K. Weber, D. Donadio, K. Landfester, S. Baluschev and F. R. Wurm, *J. Am. Chem. Soc.*, 2014, **136**, 11057–11064.

17　C. Mongin, J. H. Golden and F. N. Castellano, *ACS Appl. Mater. Interfaces*, 2016, **8**, 24038–24048.

18　D. Dzebo, K. Moth-Poulsen and B. Albinsson, *Photochem. Photobiol. Sci.*, 2017, **16**, 1327–1334.

19　Y. C. Simon and C. Weder, *J. Mater. Chem.*, 2012, **22**, 20817–20830.

20　V. Gray, K. Moth-Poulsen, B. Albinsson and M. Abrahamsson, *Coord. Chem. Rev.*, 2018, **362**, 54–71.

21　B. Joarder, N. Yanai and N. Kimizuka, *J. Phys. Chem. Lett.*, 2018, **9**, 4613–4624.

22　P. Bharmoria, H. Bildirir and K. Moth-Poulsen, *Chem. Soc. Rev.*, 2020, **49**, 6529–6554.

23　P. E. Keivanidis, S. Baluschev, T. Miteva, G. Nelles, U. Scherf, A. Yasuda and G. Wegner, *Adv. Mater.*, 2003, **15**, 2095–2098.

24　S. Baluscheva, P. E. Keivanidis, G. Wegner, J. Jacob, A. C. Grimsdale, K. Müllen, T. Miteva, A. Yasuda and G. Nelles, *Appl. Phys. Lett.*, 2005, **86**, 061904.

25　R. R. Islangulov, J. Lott, C. Weder and F. N. Castellano, *J. Am. Chem. Soc.*, 2007, **129**, 12652–12653.

26　P. B. Merkel and J. P. Dinnocenzo, *J. Lumin.*, 2009, **129**, 303–306.

27　A. Monguzzi, R. Tubino and F. Meinardi, *J. Phys. Chem. A*, 2009, **113**, 1171–1174.

28　T. N. Singh-Rachford, J. Lott, C. Weder and F. N. Castellano, *J. Am. Chem. Soc.*, 2009, **131**, 12007–12014.

29　A. Monguzzi, R. Tubino, S. Hoseinkhani, M. Campione and F. Meinardi, *Phys. Chem. Chem. Phys.*, 2012, **14**, 4322–4332.

30　R. Vadrucci, C. Weder and Y. C. Simon, *J. Mater. Chem. C*, 2014, **2**, 2837–2841.

31　R. Karpicz, S. Puzinas, V. Gulbinas, A. Vakhnin, A. Kadashchuk and B. P. Rand, *Chem. Phys.*, 2014, **429**, 57–62.

32　H. Goudarzi and P. E. Keivanidis, *J. Phys. Chem. C*, 2014, **118**, 14256–14265.

33　H. Goudarzi and P. E. Keivanidis, *ACS Appl. Mater. Interfaces*, 2017, **9**, 845–857.

34　M. Hosoyamada, N. Yanai, T. Ogawa and N. Kimizuka, *Chem. – Eur. J.*, 2016, **22**, 2060–2067.

35　T. Ogawa, M. Hosoyamada, B. Yurash, T. Q. Nguyen, N. Yanai and N. Kimizuka, *J. Am. Chem. Soc.*, 2018, **140**, 8788–8796.

36　T. Ogawa, N. Yanai, H. Kouno and N. Kimizuka, *J. Photonics Energy*, 2018, **8**, 022003.

37　K. Kamada, Y. Sakagami, T. Mizokuro, Y. Fujiwara, K. Kobayashi, K. Narushima, S. Hirata and M. Vacha, *Mater. Horiz.*, 2017, **4**, 83–87 (*J. Int. Biomed. Inf. Data*, 2018, **5**, 1219).

38　A. Abulikemu, Y. Sakagami, C. Heck, K. Kamada, H. Sotome, H. Miyasaka, D. Kuzuhara and H. Yamada, *ACS Appl. Mater. Interfaces*, 2019, **11**, 20812–20819.

39　G. M. Akselrod, P. B. Deotare, N. J. Thompson, J. Lee, W. A. Tisdale, M. A. Baldo, V. M. Menon and V. Bulovic, *Nat. Commun.*, 2014, **5**, 3646.

40　K. Narushima, S. Hirata and M. Vacha, *Nanoscale*, 2017, **9**, 10653–10661.

41　O. V. Mikhnenko, P. W. M. Blom and T. Q. Nguyen, *Energy Environ. Sci.*, 2015, **8**, 1867–1888.

42　M. Oldenburg, A. Turshatov, D. Busko, S. Wollgarte, M. Adams, N. Baroni, A. Welle, E. Redel, C. Wöll, B. S. Richards and I. A. Howard, *Adv. Mater.*, 2016, **28**, 8477–8482.

43　T. Ogawa, N. Yanai, S. Fujiwara, T. Q. Nguyen and N. Kimizuka, *J. Mater. Chem. C*, 2018, **6**, 5609–5615.

44　J. M. Rowe, J. Zhu, E. M. Soderstrom, W. Xu, A. Yakovenko and A. J. Morris, *Chem. Commun.*, 2018, **54**, 7798–7801.

45　I. Roy, S. Goswami, R. M. Young, I. Schlesinger, M. R. Mian, A. E. Enciso, X. Zhang, J. E. Hornick, O. K. Farha, M. R. Wasielewski, J. T. Hupp and J. F. Stoddart, *J. Am. Chem. Soc.*, 2021, **143**, 5053–5059.

46　M. Lusi, *CrystEngComm*, 2018, **20**, 7042–7052.

47 A. I. Kitaigorodsky, *Mixed Crystals*, Springer-Verlag, Berlin, 1984. See, e.g., the Preface and Chapter 5.

48 X. Zeng, Y. H. Huang, S. Gong, P. Li, W. K. Lee, X. Xiao, Y. Zhang, C. Zhong, C. C. Wu and C. Yang, *Mater. Horiz.*, 2021, **8**, 2286–2292.

49 M. Kubota, M. Funahashi and C. Hosokawa, European Patent EP1696015A1, 2006, URL: https://patents.google.com/patent/EP1696015A1.

50 X. F. Zhang, Q. Xi and J. Zhao, *J. Mater. Chem.*, 2010, **20**, 6726–6733.

51 J. Kalinowski, W. Stampor, J. Szmytkowski, M. Cocchi, D. Virgili, V. Fattori and P. D. Marco, *J. Chem. Phys.*, 2005, **122**, 154710.

52 Y. Zhou, F. N. Castellano, T. W. Schmidt and K. Hanson, *ACS Energy Lett.*, 2020, **5**, 2322–2326.

53 Y. Murakami and K. Kamada, *Phys. Chem. Chem. Phys.*, 2021, **23**, 18268–18282.

54 Reference Air Mass 1.5 Spectra, ASTM G-173-03, https://www.nrel.gov/grid/solar-resource/spectra-am1.5.html.

55 R. Mason, *Acta Crystallogr.*, 1964, **17**, 547–555.

56 J. M. Adams and S. Ramdas, *Acta Crystallogr.*, 1979, **B35**, 679–683.

57 I. A. Baburin and V. A. Blatov, *Acta Crystallogr.*, 2004, **B60**, 447–452.

58 X. Li and M. L. Tang, *Chem. Commun.*, 2017, **53**, 4429–4440.

59 A. Monguzzi, J. Mezyk, F. Scotognella, R. Tubino and F. Meinardi, *Phys. Rev. B: Condens. Matter Mater. Phys.*, 2008, **78**, 195112.

60 S. Raišys, K. Kazlauskas, S. Juršėnas and Y. C. Simon, *ACS Appl. Mater. Interfaces*, 2016, **8**, 15732–15740.

61 S. Raišys, O. Adomėnieni, P. Adomėnas, A. Rudnick, A. Köhler and K. Kazlauskas, *J. Phys. Chem. C*, 2021, **125**, 3764–3775.

62 N. J. Turro, V. Ramamurthy and J. C. Scaiano, *Principles of Molecular Photochemistry: An Introduction*, University Science Books, Sausalito, CA, USA, 2009, pp. 396–413.

63 Section 17.1 of A. E. Siegman, *Lasers*, University Science Books, Sausalito, CA, USA, 1986.